Materials Characterization 230 (2025) 115768

Contents lists available at ScienceDirect

Materials Characterization

journal homepage: www.elsevier.com/locate/matchar

Role of Ni in high elastic modulus Al-Si-Ni alloys: Solidification and microstructure evolution

Yoon-Ho Lee [a,b], Saif Haider Kayani [a], Jung-Moo Lee [a], Sang-Ik Lee [a,b], Jae-il Jang [b], Young-Hee Cho [a,*]

[a] Lightweight Materials Research Division, Korea Institute of Material Science, Changwon 51508, Republic of Korea
[b] Department of Materials Science and Engineering, Hanyang University, Seoul 04763, Republic of Korea

ARTICLE INFO

Keywords:
Hypereutectic Al-Si alloy
Ni addition
Ni-rich intermetallic compound (Ni-rich IMC)
Solidification
Microstructure

ABSTRACT

A novel Al-Si-Ni casting alloy with an ultra-high elastic modulus exceeding 100 GPa was developed by compositional tailoring of a hypereutectic Al-18Si binary system through incremental Ni addition from 4 to 28 wt %. The solidification behavior and microstructural evolution were systematically investigated with respect to Ni content, focusing on the formation and morphology of Ni-rich intermetallic compounds (IMCs) and the refinement of primary Si (Si_p) particles. When the Ni content exceeded 8 wt%, Si_p and primary Al_3Ni formed sequentially in the first stage of solidification, followed by the Al–Si-Al_3Ni eutectic reaction. At Ni content exceeding 20 wt%, the Al_6Ni_3Si (τ_3) was formed as a primary phase, and it was observed to exist as a binary mixture of Al_3Ni-Al_6Ni_3Si with a core-shell structure. In addition, the nucleation temperature of Si_p rises, weakening the refinement effect of AlP and resulting in the coarsening of Si_p. With further addition to 24 wt% Ni, the Al_3Ni_2 was formed as a primary phase, and a ternary mixture with a distinct layered morphology appeared, consisting of Al_3Ni_2, Al_6Ni_3Si, and Al_3Ni phases. Transmission electron microscopy (TEM) analyses revealed crystallographic orientation relationships between these IMCs: (110)[$\bar{1}$13] Al_6Ni_3Si // (0$\bar{3}$1)[$\bar{1}$13] Al_3Ni and (0$\bar{1}$13)[$\bar{1}$2$\bar{1}$1] Al_3Ni_2 // (100)[031] Al_6Ni_3Si. Based on these observations, the phase formation sequence and microstructural evolution mechanisms during solidification were elucidated as a function of Ni content, which provides fundamental guidance for designing high-modulus lightweight alloys with optimized microstructures.

1. Introduction

Reducing vehicle weight can be accelerated by substituting traditional steel parts with Al-Si casting alloys, which offer excellent castability, good high-temperature strength, a low coefficient of thermal expansion, and mechanical properties comparable to steel [1–4]. However, for critical structural applications such as ride-control and handling components, Al-Si alloys must achieve an elastic modulus comparable to that of steel (~210 GPa) [5–7]. Commercial hypereutectic Al-Si alloys exhibit relatively high elastic modulus values (~80 GPa), surpassing those of pure Al and most general-purpose Al alloys (~70 GPa). This enhancement is attributed to the stiffening effect of hard primary Si (Si_p), which form during the early stage of solidification. It is estimated that primary and eutectic Si particles increase the elastic modulus by approximately 1.6 GPa and 0.4 GPa per vol%, respectively [8]. However, increasing the Si content to raise the fraction of Si_p often results in reduced ductility, presenting a significant trade-off between stiffness and toughness.

To overcome this trade-off, various approaches have been proposed to further enhance the modulus of Al-Si alloys without compromising ductility [4,6–11]. These include the incorporation of reinforcing ceramic phases and metastable precipitates. Nevertheless, the poor wettability, brittleness, and interfacial instability of reinforcing particles frequently hinder their uniform dispersion and limit their strengthening effectiveness [10,12]. In addition, although metastable precipitation *via* heat treatment can modify microstructures, it has been reported to decrease the modulus due to the removal or redistribution of stiff phases [8]. Recent studies suggest that alloying additions can simultaneously reduce the Si particle fraction while enhancing the modulus. Among candidate elements, Ni has attracted considerable attention due to its low solid solubility in Al, which promotes the formation of Ni-rich intermetallics such as Al_3Ni, Al_3Ni_2, Al_9Ni_2, and Al_4Ni_3 [13,14]. The

* Corresponding author.
E-mail address: y.cho@kims.re.kr (Y.-H. Cho).

https://doi.org/10.1016/j.matchar.2025.115768
Received 28 August 2025; Received in revised form 4 November 2025; Accepted 6 November 2025
Available online 8 November 2025

addition of Ni has been reported to increase the modulus of Al by approximately 1.08–1.16 GPa per wt% [11,15], and by as much as ~1.9 GPa per wt% in Al-Si casting alloys *via* the formation of Al_3Ni [16]. Based on these findings, we recently developed an Al-18Si-8Ni alloy exhibiting an elastic modulus of ~95 GPa [4]. In addition to improving stiffness, Ni also enhances thermal stability by reducing the coefficient of thermal expansion, while exerting minimal influence on electrical conductivity [17–19]. Thus, these investigations suggest that Al-Si-Ni alloys are promising candidates for achieving modulus values exceeding 100 GPa.

However, the addition of Ni to a binary Al-Si system may also lead to the formation of ternary intermetallic phases at specific compositions. While the thermodynamics of intermetallic formation in the Al-Si-Ni system have been previously investigated, most studies have focused on hypoeutectic alloys (Si < 12.6 wt%, Ni < 6.1 wt%) [20–27], and limited data are available for hypereutectic systems. Raghavan et al. [21] reported the crystal structures and compositions of several ternary phases in the Al-Si-Ni system, including $Al_{13}Ni_{67}Si_{20}$, $AlNi_2Si$, Al_6Ni_3Si, $Al_ySi_{9-y}Ni_{13+x}$, and $AlNi_{16}Si_9$. Xiong et al. [22] calculated the formation enthalpies of $Ni_2(Al, Si)$, Al_6Ni_3Si, $Al_ySi_{9-y}Ni_{13+x}$, $AlNi_{16}Si_9$, $Ni_5(Al, Si)_3$, and $(Al, Ni)Si_4$ and constructed ternary phase diagrams over different temperature ranges. Liu et al. [23] investigated the effect of Ni content on the microstructure, physical properties and thermal behavior of Al-22Si-xNi alloys (x = 0–20 wt%) and observed the transient formation Al_6Ni_3Si during solidification; though its persistence and influence on properties remained unclear. In particular, the mechanisms underlying the consumption and transformation of ternary phases at high Ni contents have not been sufficiently explained, highlighting the need for a more systematic understanding of phase stability and solidification behavior.

To address these gaps, this study aims to investigate the effects of Ni content on the microstructural evolution and phase formation in hypereutectic Al-18Si-xNi alloys.

Specifically, we explore the solidification pathways and formation mechanisms of Ni-rich intermetallic phases, their crystallographic orientation relationship, and thermodynamic stability. Through this analysis, we seek to elucidate the fundamental mechanisms governing solid-state transformations during solidification and provide guidance for the design of high-modulus Al-Si-Ni casting alloys.

2. Experimental

Al-18Si-xNi (wt%) alloys with Ni contents ranging from 4 to 28 wt% were prepared using a steel step mold, following the procedure described in [4] and Fig. S1. Table 1 lists the chemical compositions of the alloys measured by inductively coupled plasma optical emission spectrometry (ICP-OES).

Microstructural characterization was carried out using an optical microscope (OM, MA200, Nikon) and a field emission scanning electron microscope (FE-SEM, Mira 1 LHM, TESCAN). Energy dispersive spectroscopy (EDS), electron backscatter diffraction (EBSD), and X-ray diffraction (XRD) were employed to identify the IMCs. XRD was conducted on a Malvern Panalytical diffractometer with Cu-Kα radiation (1.54 Å), over a scanning angle (2θ) range of 10° to 140°, using a step size of 0.0131°. Phase identification was carried out using ICDD cards, and crystallographic information was obtained from references [24, 28, 29] (Table 2). The crystallographic features of the IMC phases were examined by a spherical aberration Cs-corrected transmission electron microscope (TEM, Themis Z, Thermo Fisher Scientific) operating at 300 keV. TEM samples were prepared using a focused ion beam (FIB, Scios2, Thermo Fisher Scientific). The obtained ingots were cut into 40 × 15 × 3 mm specimens for measuring elastic modulus. Dynamic Young's modulus *E* (GPa) of alloys was determined by the Impulse Excitation Technique (IET) according to ASTM E1876 [30].

Table 1
Chemical compositions of the investigated Al-18Si-xNi alloys (wt%).

Alloy code	Si	Ni	Mg	Fe	Ti	P	Al
4Ni	18.3	4.76	0.39	0.08	0.04	100 ppm	Bal.
8Ni	17.7	8.74	0.41	0.08	0.04	100 ppm	Bal.
12Ni	17.9	12.1	0.39	0.08	0.04	100 ppm	Bal.
16Ni	17.7	17.2	0.41	0.07	0.04	100 ppm	Bal.
20Ni	17.4	20.1	0.38	0.09	0.05	100 ppm	Bal.
22Ni	17.7	22.7	0.38	0.07	0.04	100 ppm	Bal.
24Ni	17.3	24.6	0.41	0.08	0.05	100 ppm	Bal.
26Ni	18.0	26.2	0.39	0.06	0.03	100 ppm	Bal.
28Ni	18.6	28.6	0.42	0.06	0.03	100 ppm	Bal.

3. Results

3.1. Solidification behavior and phase formation in Al-18Si-xNi alloys

Fig. 1 and Fig. S2 show Scheil simulations of Al-18Si-xNi alloy with four different levels of Ni predicting phases in the early stage of solidification using Thermo-Calc with TCAL8 database [31]. The solidification sequence corresponding to each alloy shown in Fig. 1 is presented in Table 3 In the 4Ni and 16Ni alloys, solidification starts with the formation of Si_p at 672 and 709 °C, followed by the formation of primary Al_3Ni and α-Al (Fig. 1(a) and (b)). When increasing the Ni to 22 wt% (22Ni), primary Al_6Ni_3Si begins to form first at 745 °C prior to the formation of Si_p, and then solidification proceeds similarly to the 4Ni and 16Ni alloys (Fig. 1(c)). It is also predicted that the primary Al_6Ni_3Si is consumed, leading to the formation of primary Al_3Ni and Si_p *via* a U-type transition reaction [22,24] or a quasi-peritectic reaction, in which the liquid phase reacts with the existing Al_6Ni_3Si phase to simultaneously produce Al_3Ni and Si. This reaction exhibits characteristics of both peritectic ($L + \alpha \rightarrow \beta$) and eutectic transformations ($L \rightarrow \alpha + \beta$), as described in [23]:

$$\text{Liquid} + Al_6Ni_3Si\ (\tau_3) \rightarrow Al_3Ni + Si \quad (1)$$

As shown in Fig. 1(d), the solidification of the 28Ni alloy initiates at an even higher temperature of 821 °C with the formation of primary Al_3Ni_2, followed by the serial formation of primary Al_6Ni_3Si, Si_p, Al_3Ni and α-Al, similarly to the 22Ni alloy. It should be noted, however, that the primary Al_3Ni_2 is no longer observed in the later stages of solidification (Stage 3 to 5 in Table 3), as it undergoes a transition reaction [22,24]:

$$\text{Liquid} + Al_3Ni_2 \rightarrow Al_6Ni_3Si + Si \quad (2)$$

Fig. 2 shows optical micrographs of as-cast Al-18Si–xNi alloys with various Ni amounts, commonly consisting of Si_p particles in black and Ni-rich IMCs in gray. As the Ni content increases from 4 to 16 wt%, both the size and the volume fraction of Ni-rich IMCs increase significantly. It can also be seen in Fig. 2 that, besides the polygonal-shaped Si_p, rather coarser ellipsoidal primary Al_3Ni was found to form in the alloys with Ni content exceeding 8 wt%. Once the Ni content exceeds 20 wt%, the morphology of the Ni-rich IMCs changes significantly. For example, the IMCs in the 20Ni and 22Ni alloys exhibit a cloud-like morphology. At 24 wt% Ni, the cloud-like IMCs begin to disappear, and needle-like IMCs start to form. The cloud-like IMCs have completely disappeared at 26 wt % Ni.

To further verify the effect of Ni addition on the stiffness, the elastic modulus of Al-18Si-xNi alloys were measured in accordance with ASTM E1876 [30], and the results are summarized in Table. 4. As the Ni content increased, the elastic modulus gradually rose from 86.21 GPa, with an average increment rate of approximately 1.45 GPa per Ni wt%, exceeding 100 GPa at 16 wt% Ni. However, in the composition range where cloud-like IMCs formed (20–22 wt%), the elastic modulus increased more steeply, at a rate of about 1.84 GPa per Ni wt%. In addition, for compositions where needle-like IMCs formed (≥ 24 wt%), the increase in elastic modulus became more moderate, suggesting that the morphological evolution of Ni-rich IMCs with Ni addition is closely

Table 2
Crystallographic data of constituent phases in the Al-18Si-xNi alloys.

Phase	Crystal structure	Space group	Lattice parameters	V_{Cell} (Å^3)	Density(g/cm^3)	Ref
Al	FCC	Fm$\bar{3}$m (225)	a = b = c = 4.0515 Å, α = β = γ = 90 °	66.50	2.7	[28]
Si	Cubic	Fd$\bar{3}$m (227)	a = b = c = 5.432 Å, α = β = γ = 90 °	160.28	2.33	[24]
Al_3Ni	Orthorhombic	Pnma (62)	a = 6.618, b = 7.386, c = 4.814 Å, α = β = γ = 90 °	235.31	3.95	[29]
Al_6Ni_3Si	Cubic	Im$\bar{3}$m (229)	a = b = c = 8.3159 Å, α = β = γ = 90 °	575.08	4.23	[24]
Al_3Ni_2	Trigonal	P$\bar{3}$m1 (164)	a = b = 4.0365 Å, c = 4.9003 Å α = β = 90°, γ = 120 °	69.15	4.76	[24]

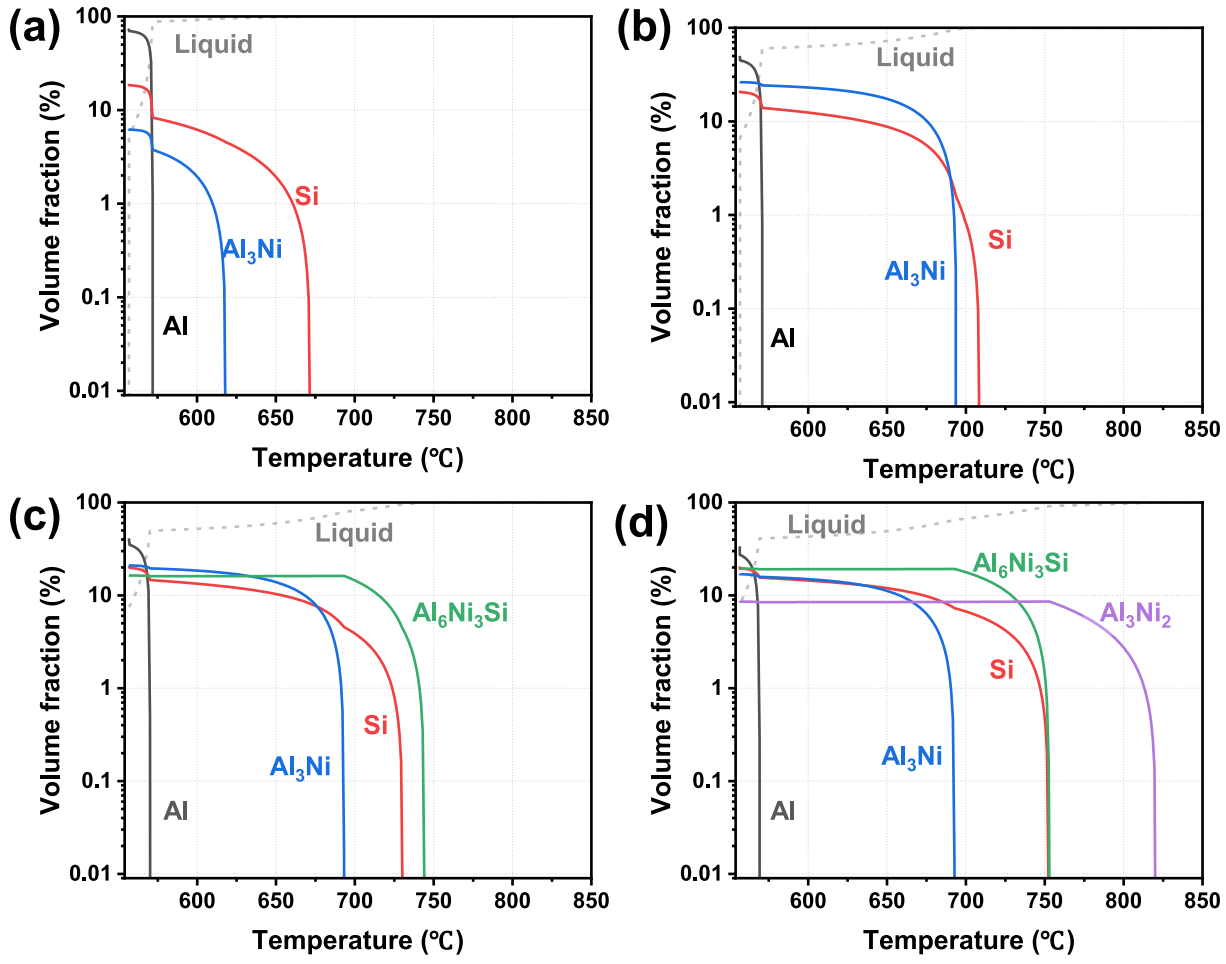

Fig. 1. Scheil simulations predicting the solidification sequence of Al-18Si-xNi alloys in the early stage of solidification using Thermo-Calc with TCAL8 database [31]: (a) 4Ni; (b) 16Ni; (c) 22Ni; and (d) 28Ni.

related to the variation in the alloy's stiffness.

Figs. 3(a) and (b) shows the enlarged micrographs showing Ni-rich IMCs with cloud-like and needle-like structures observed in the 22Ni and 28Ni alloys, respectively. Both morphologies show a sharp contrast between phases, indicating the presence of multiple phases. The cloud-like IMCs exhibit a core-shell structure, in which a polygonal dark gray phase is surrounded by a light gray shell. On the other hand, the needle-like IMCs have a layered structure consisting of a black core, a dark gray intermediate layer, and an outmost light gray layer. (Hereafter referred to as core-shell and layered structure, respectively.)

It is also clear from Fig. 2 that the overall blocky morphology of Si_p remains constant while its size changes with Ni content. As evidenced in Fig. 3(c), the Si_p size is 30–40 μm when the Ni content is 4 to 16 wt%, and increases sharply to ~60 μm at 20 wt%Ni. When the Ni content exceeds 20 wt%, the Si_p size stabilizes in the range of 55–70 μm. This coarsening behavior can be interpreted as resulting from changes in the nucleation temperature of the phase refiner (AlP) and Si_p, depending on the Ni content, as shown in Fig. 3(b) [32]. As the Ni content increase, the nucleation temperature of Si_p rises from 663 to 776 °C, despite a constant Si content. This is because Al content decrease as the amount of alloying additions increase, leading to a higher Si_p nucleation temperature under hypereutectic conditions. In contrast, the nucleation temperature of AlP remains relatively stable, as the P content is very low (100 ppm), despite varying Ni-to-Al ratios [33]. At 20 wt% Ni, the nucleation temperature of Si_p exceeds that of AlP. Although AlP typically acts as an effective refiner for Si_p, its refining effect diminishes or disappears when its nucleation temperature becomes lower than that of Si_p, resulting in coarser Si particles.

Table 3
Scheil simulations predicting reaction sequences of the Al-18Si-xNi alloys in the early stage of solidification using Thermo-Calc with a TCAL8 database [31] as depicted in Fig. 1.

Stage	4Ni and 16Ni	22Ni	28Ni
1	Si + Liq. At 672 °C (4Ni), 709 °C (16Ni)	Al_6Ni_3Si + Liq. At 745 °C	Al_3Ni_2 + Liq. At 821 °C
2	Al_3Ni + Si + Liq. At 619 °C (4Ni), 694 °C (16Ni)	Si + Al_6Ni_3Si + Liq. At 731 °C	Al_6Ni_3Si + Al_3Ni_2 + Liq. At 753 °C
3	α-Al + Al_3Ni + Si + Liq. At 572 °C (4Ni), 571 °C (16Ni)	Al_3Ni + Si + Liq. At 694 °C	Si + Al_6Ni_3Si + Liq. At 753 °C
4	–	α-Al + Al_3Ni + Si + Liq. At 571 °C	Al_3Ni + Si + Liq. At 693 °C
5	–	–	α-Al + Al_3Ni + Si + Liq. At 570 °C

3.2. Phase identification and quantification of Ni-rich IMCs

To further investigate the morphologies Ni-rich IMCs, we performed SEM and EDS analyses on Al-18Si-xNi alloys (Fig. 4). As shown in Fig. 4 (a, b), skeleton-like and granular IMCs were identified in the 4Ni and 16Ni alloys, respectively. Elemental mapping revealed no overlap between Ni and Si, indicating that the Si-rich particles correspond to Si_p, while the Ni-rich particles are Al_3Ni. In contrast, the 22Ni alloy contained core-shell IMCs with compositional gradients within individual particles. Specifically, the particle exteriors were relatively Ni-lean and exhibited higher Si content, as highlighted by the white arrows in Fig. 4(c). Similarly, the layered structure IMCs observed in the 28Ni alloy displayed Ni-rich interiors and Ni-lean exteriors; again, the exteriors showed elevated Si content (Fig. 4(d)). These findings suggest that once the Ni content exceeds approximately 20 wt%, the IMCs particles have morphologies wherein multiple IMC phases may coexist within a single particle.

Fig. 5 presents the image quality (IQ; a, d), phase (b, e), and inverse pole figure (IPF; c, f) maps for the 22Ni (a–c) and 28Ni (d–f) alloys. In the 22Ni alloy, the IQ map (Fig. 5 (a)) illustrates distinct contrast in the intermetallic compound (IMC) phases, consistent with the SEM observation. The phase map (Fig. 5 (b)) indicates a core-shell structure comprising an Al_6Ni_3Si core and an Al_3Ni shell. Notably, some particles

Table 4
Variation of elastic modulus, density, and specific modulus with Ni content in Al-18Si-xNi.

Properties	Al-18Si-xNi alloys			
	4Ni	16Ni	22Ni	28Ni
Elastic modulus, E (GPa)	86.21	103.63	114.68	123.51
Density (g/cm^3)	2.73	2.96	3.17	3.23
Specific modulus (10^6 m^3/s^2)	31.58	35.01	36.18	38.24

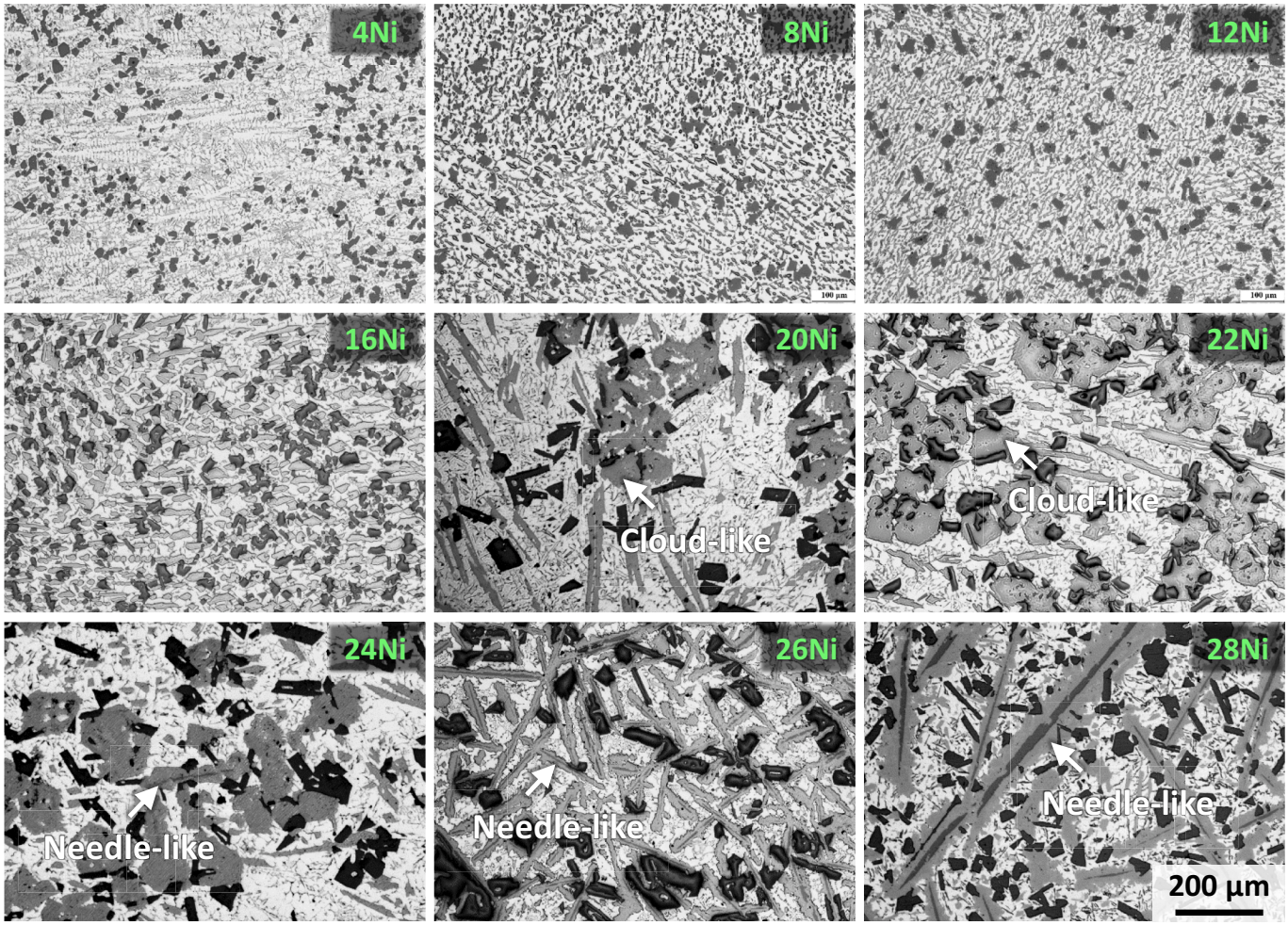

Fig. 2. OM images showing microstructures of the Al-18Si-xNi alloys with the addition of Ni ranging from 4 to 28 wt%.

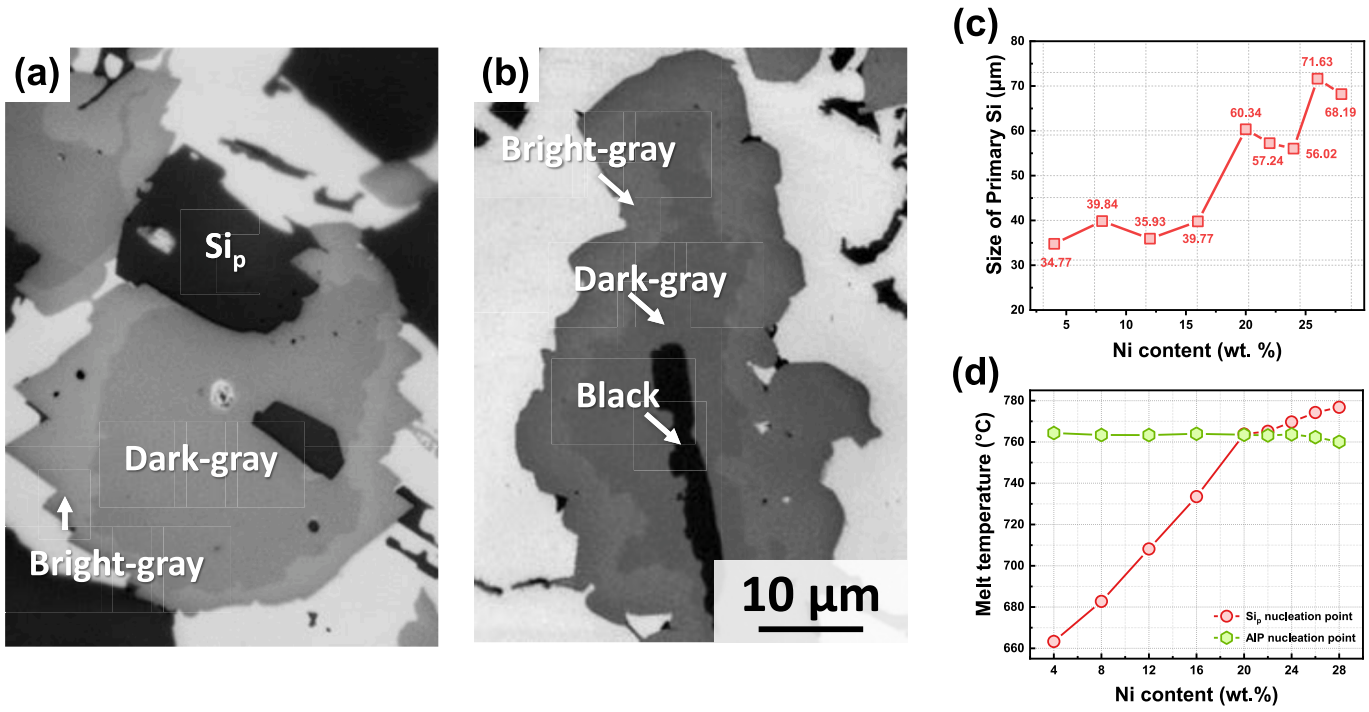

Fig. 3. Ni-rich intermetallic compounds (IMCs) exhibiting (a) a cloud-like structure in the 22Ni alloy and a needle-like structure in the 28Ni alloy. (b) Change in the size of primary Si (Si_p) size and (d) nucleation temperature of Si_p and AlP, calculated using a FactSage software with FTlite database [32].

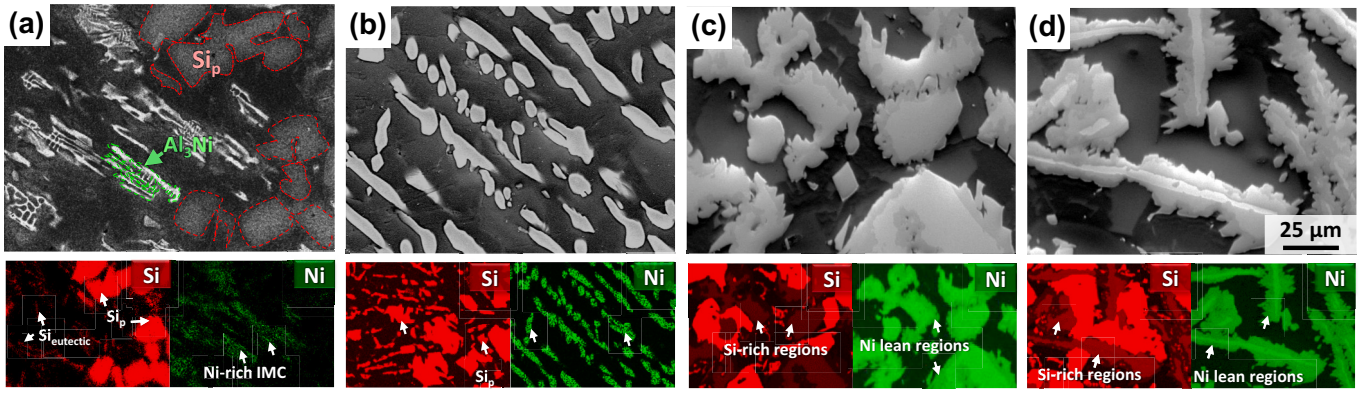

Fig. 4. SEM images and corresponding EDS mapping of Al-18Si-xNi alloys: (a) 4Ni; (b) 16Ni; (c) 22Ni alloy with a core-shell IMCs; and (d) 28Ni alloy with needle-like IMCs having a layered structure.

deviate from this structure, showing Si instead of Al_3Ni as the shell phase and the Al_6Ni_3Si core (highlighted by the white dotted line). The IPF map (Fig. 5 (c)) reveals that the Al_6Ni_3Si core has a single crystallographic orientation, acting as a substrate for shell growth, whereas the shell consists of multiple grains with varying orientations (white arrows). In the 28Ni alloy, the IQ map (Fig. 5 (d)) similarly shows clear contrast between IMC phases. The phase map (Fig. 5 (e)) identifies all layered particles as comprising an Al_3Ni_2 core, an intermediate Al_6Ni_3Si layer, and an outer Al_3Ni shell. Interestingly, the Al_6Ni_3Si and Al_3Ni_2 phases appear intermingled, suggesting a possible inter-diffusion between the two phases during formation. The IPF map (Fig. 5(f)) confirms that the Al_3Ni_2 core exhibits a single orientation, while the surrounding layers contain multiple grain orientations (indicated by white arrows. These results demonstrate that both the solidification behavior and resulting IMC morphology in Al-18Si-xNi alloys are strongly affected by Ni content. Furthermore, the observed structures support a hypothesis that diffusion-driven formation occurs between the Ni-rich phases during solidification.

Fig. 6 presents the XRD patterns of the Al-18Si–xNi alloys. All alloys exhibit high-intensity peaks at 28.43° and 38.45°, corresponding to the (111) planes of Si and Al, respectively. In addition, several low-intensity peaks associated with the orthorhombic Al_3Ni phase are observed. Due to its low symmetry and numerous distinct diffraction planes, Al_3Ni produces multiple peaks, and its intensities increase with increasing Ni content. As shown in Fig. 6(b), the (011), (101), and (111) peaks of Al_3Ni become more prominent as the Ni content increases to 16 wt%. When the Ni content reaches 20 wt%, additional peaks appear at 21.35°, 26.22°, 40.71°, and 53.97°, respectively corresponding to the (200), (211), (321), and (411) planes of Al_6Ni_3Si. Al_6Ni_3Si has a cubic crystal structure with space group $Im\bar{3}m$ [24]. Furthermore, at Ni content reaches of 24 wt%, and higher, new peaks are observed at 18.08° and 31.40°, associated with the (001) and (011) planes of Al_3Ni_2 which has a trigonal structure with space group $P\bar{3}m1$ [24].

The phase fractions of Al-18Si-xNi alloys were quantified by the derivative difference minimization method using XRD data. The quantified fractions for the Al-matrix, Si, Al_3Ni, Al_6Ni_3Si, and Al_3Ni_2 phases

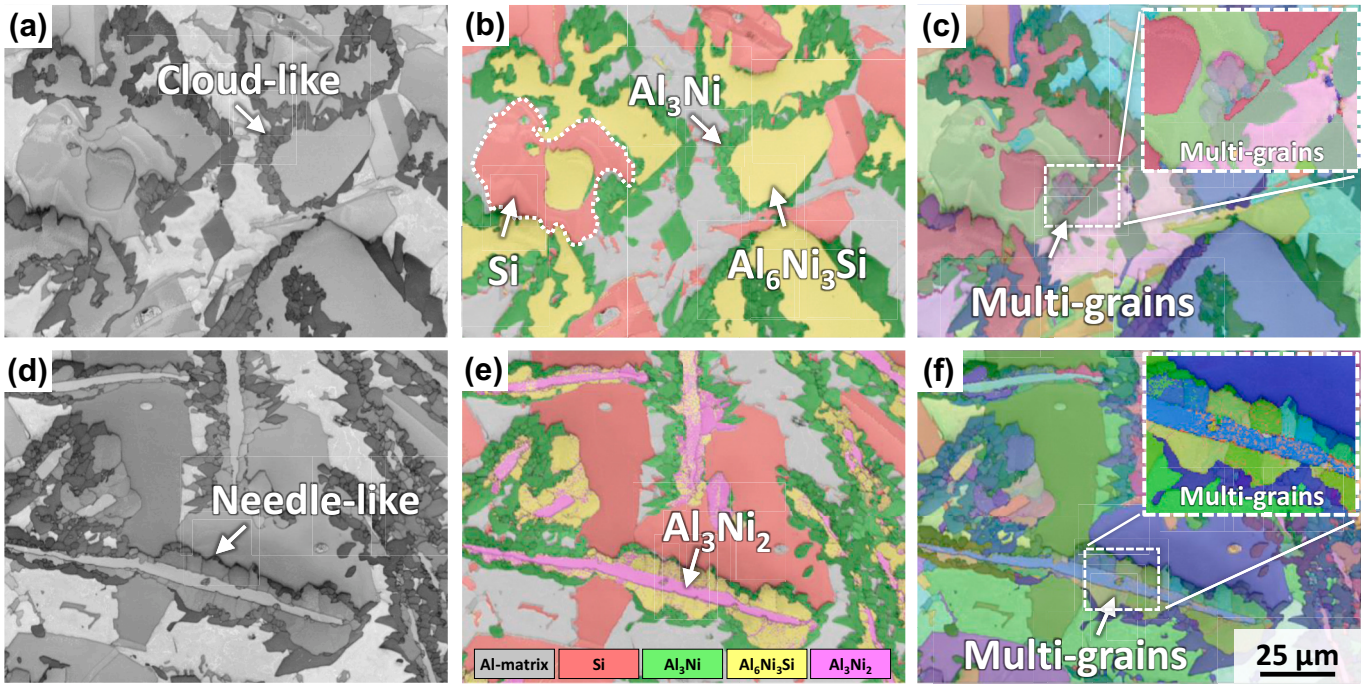

Fig. 5. Electron backscatter diffraction (EBSD) results of (a-c) the 22Ni and (d-f) the 28Ni alloys: (a, d) image quality (IQ) map; (b, e) phase map; and (c, f) inverse pore figure (IPF).

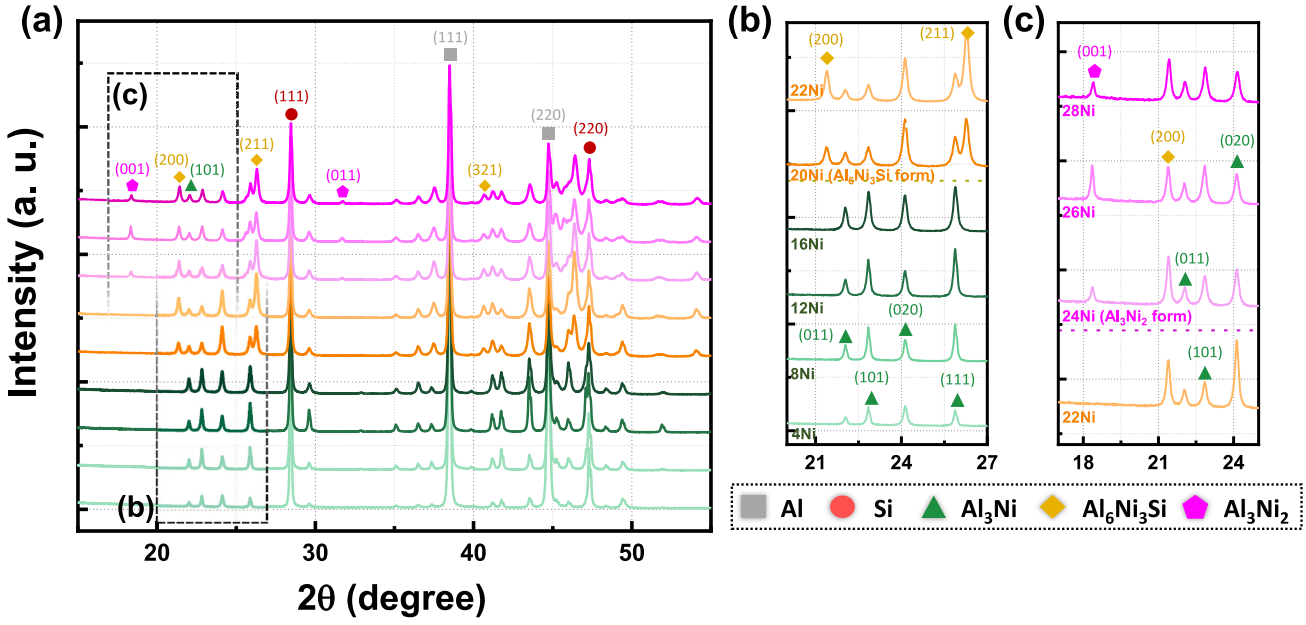

Fig. 6. X-ray diffraction patterns of (a) Al-18Si-xNi alloys; (b) compositions at which Al_6Ni_3Si phase forms, along with the low-angle diffraction patterns for lower Ni contents; (c) compositions at which Al_3Ni_2 phase forms, along with the low-angle diffraction patterns for lower Ni contents.

are shown in Fig. 7(a). Al_3Ni is the only Ni-rich IMC phase formed in the 4–16 Ni alloys, and its volume fraction increases with Ni content, reaching a maximum of 18.22 vol% in the 16Ni alloy. In the 20Ni alloy, the Al_6Ni_3Si phase begins to form while Al_3Ni fraction decreases to 15.18 vol%. Then, the Al_3Ni fraction slightly increases to 16.34 vol% in the 22Ni alloy. When Ni is added more than 24 wt%, Al_3Ni_2 phase starts to form, and its volume fraction is unlikely to change with the increase in Ni content. This is somewhat different from the microstructural analysis result in Fig. 2, and this discrepancy in the phase quantification by XRD possibly comes from several factors such as the severity of segregation, particle size of the phases and peak overlapping. Fig. 7(b) shows the thermodynamic calculations (Scheil simulations) predicting the phase fractions of the Al-18Si-xNi alloys using Thermo-Calc software and the TCAL8 database [31]. Unlike the IMC fraction analysis using XRD data, thermodynamic calculations predict a continuous decrease in the volume fraction of Al_3Ni due to the formation of Al_6Ni_3Si, and a decrease in the volume fractions of both Al_3Ni and Al_6Ni_3Si due to the formation of Al_3Ni_2.

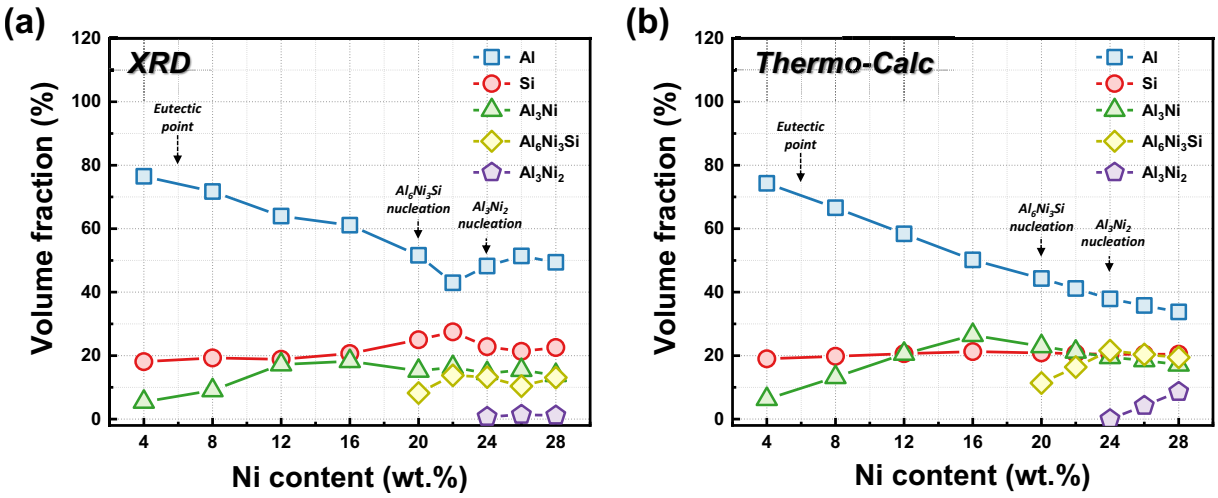

Fig. 7. Volume fractions of constituent phases in Al-18Si-xNi alloys: (a) estimated by XRD analysis and (b) calculated by Scheil simulations [31].

4. Discussions

4.1. Phase transformation mechanisms in the Al-18Si-xNi alloys

The addition of Ni to Al-18Si alloys induces significant changes in the type, volume fraction, and morphology of Ni-rich IMCs. When the Ni content exceeds a threshold level, typically above ~20 wt%, the microstructure evolves from single Al_3Ni phase to more complex multi-phase structures containing Al_6Ni_3Si and Al_3Ni_2. These IMCs are formed through a series of sequential solidification events both primary nucleation and phase transformations.

Fig. 8 shows the liquidus projection of the Al-Si-Ni phase diagram calculated using Thermo-Calc with TCAL8 database [31]. The segregation lines (dotted lines) during solidification of the Al-18Si-16Ni, 22Ni, and 28Ni are calculated using Scheil simulations and are also superimposed over Fig. 8. It is clear from Fig. 8 that the solidification sequences of the Al-18Si-xNi alloys are highly sensitive to the Ni content, indicating the initial formation of Si, Al_6Ni_3Si, and Al_3Ni_2 as primary phase at 16 wt%Ni, 22 wt%Ni and 28 wt%Ni, respectively. In the 16Ni alloy, the solidification begins with the sequential formation of Si_p and primary Al_3Ni, followed by a ternary Al-Si-Al_3Ni eutectic reaction. When increasing the Ni content to 22 wt%, primary Al_6Ni_3Si, which is designated as τ_3 [24] and Si_p form sequentially. The subsequent formation of Al_3Ni is likely to occur *via* a quasi-peritectic reaction [23] or a U-type transition reaction [24] (Liq. + Al_6Ni_3Si = Al_3Ni + (Si)) and the solidification is finally terminated in the ternary Al-Si-Al_3Ni eutectic reaction. In the 28Ni alloy, solidification initiates with primary Al_3Ni_2 and primary Al_6Ni_3Si formation and then goes through a transition reaction (Liq. + Al_3Ni_2 = Al_6Ni_3Si + (Si)) [24]. Similar to the 22Ni alloy, following reaction upon solidification of the 28Ni alloy undergoes the quasi-peritectic and the ternary eutectic reactions subsequently.

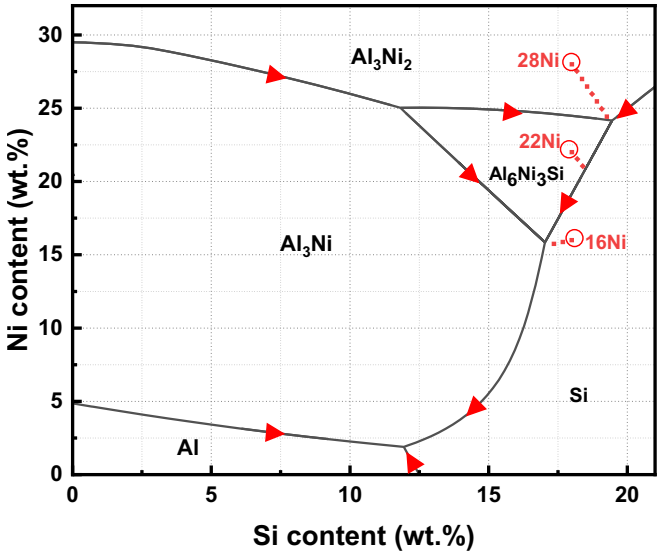

Fig. 8. Solidification paths across the liquidus projection of the equilibrium Al-Si-Ni ternary phase diagram [31].

The solidification pathways derived from Fig. 8, in conjunction with the microstructures shown in Fig. 5, suggest that the phase transformations occurring in the 22Ni and the 28Ni alloys in the early stage of solidification are more likely to reflect quasi-peritectic reactions involving interfacial nucleation and diffusion-driven growth. In order to confirm the reactions upon solidification, particularly the nucleation event, orientation relationship between the Ni-rich IMCS in the core-shell structure (22Ni alloy) and layered structure (28Ni alloy) were analyze using TEM and the results are presented in Fig. 9 and Fig. 10, respectively. In the 22Ni alloy, Figs. 9(a) and (b) show bright field (BF) TEM images exhibiting Al_6Ni_3Si core surrounded by multi grains of Al_3Ni shells. The EDS maps in Fig. 9(c) and a high resolution (HR) TEM image (Fig. 9(d)) along with the diffraction pattern analysis (Fig. 9(e)) confirm the presence of a distinct interphase phase boundary between Al_6Ni_3Si and Al_3Ni of the core-shell structure (see the crystallographic data in Table 2). More importantly, a selected area diffraction pattern obtained by fast Fourier transform (FFT) in Fig. 9(e) reveals a crystallographic orientation relationship (OR) between Al_6Ni_3Si and Al_3Ni: (110)[$\bar{1}$13] Al_6Ni_3Si // (0$\bar{3}$1)[$\bar{1}$13] Al_3Ni. It is also clear from Fig. 9(f) that the (110) Al_6Ni_3Si and (0$\bar{3}$1) are parallel to each other with an approximately 7° misorientation angle, indicating that Al_3Ni nucleates epitaxially on the Al_6Ni_3Si substrate *via* a quasi-peritectic reaction [34]. Based on the HR TEM results and the simulated atomic arrangements (see electronic Supplementary Fig. S3), lattice misfit between the phases was calculated by Edge-to-Edge model [34,35], which reveals the interatomic mismatch of 4.95 % along [$\bar{1}$13] Al_6Ni_3Si and [$\bar{1}$13] Al_3Ni. This is consistent with acceptable OR conditions for interfacial nucleation (typically less than 10 %).

In the 28Ni alloy, layered IMC particles are observed with a primary Al_3Ni_2 core, an intermediate Al_6Ni_3Si layer, and an outer Al_3Ni shell (Fig. 5(e) and Fig. 10(a)). The HR TEM image in Fig. 10(b) shows the interface between Al_3Ni_2 and Al_6Ni_3Si, while FFT in the inset indicates the OR of (0$\bar{1}$13)[$\bar{1}$2$\bar{1}$1] Al_3Ni_2 // (100)[031] Al_6Ni_3Si. As evidenced in Fig. 10(c), an inverse FFT exhibits a parallel plane between Al_3Ni_2 and

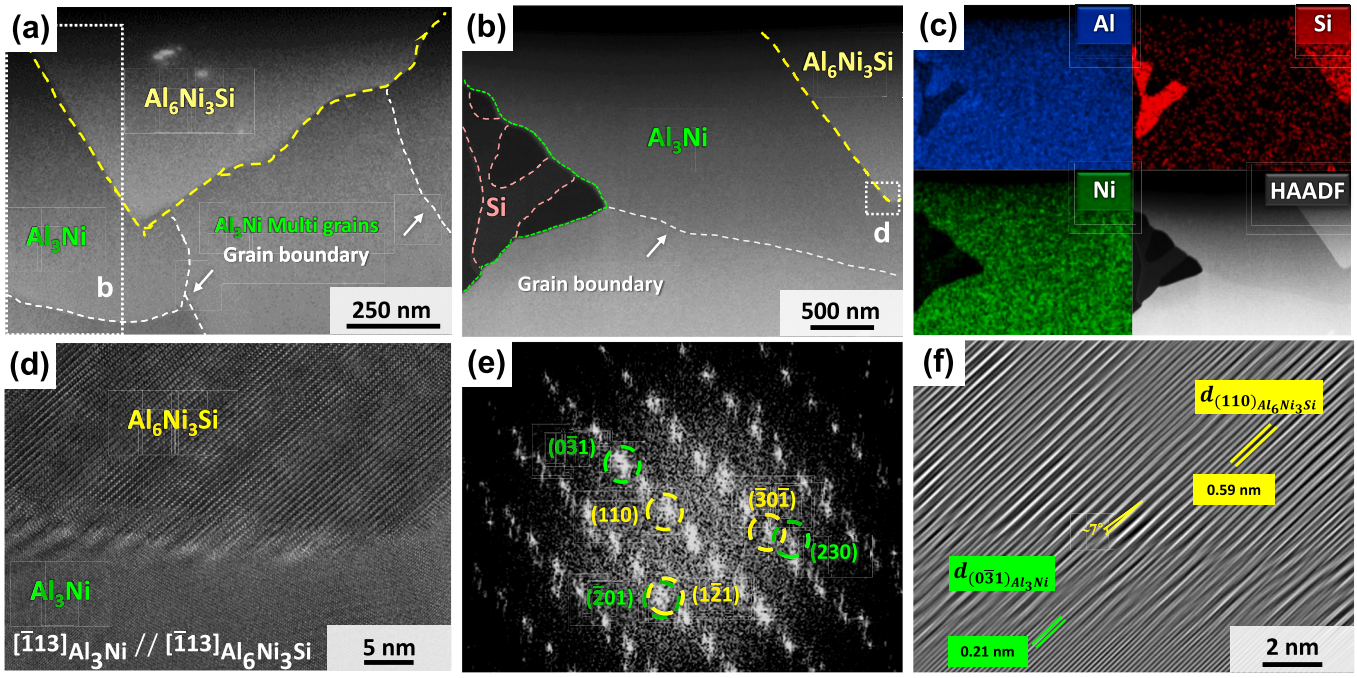

Fig. 9. (a, b) Scanning transmission electron microscopy (STEM) bright-field (BF) images showing an Al_6Ni_3Si core surrounded by multi grains of Al_3Ni shells in the 22Ni alloy and (c) EDS elemental maps corresponding (b). (d) High-resolution (HR) TEM image and the (e) corresponding fast Fourier transform (FFT; inset) showing the orientation relationship: $[\bar{1}13]$ Al_3Ni ‖ $[\bar{1}13]$ Al_6Ni_3Si. (f) Inverse FFT image showing the interface between Al_3Ni and Al_6Ni_3Si phases along $(0\bar{3}1)$ Al_3Ni and (110) Al_6Ni_3Si planes.

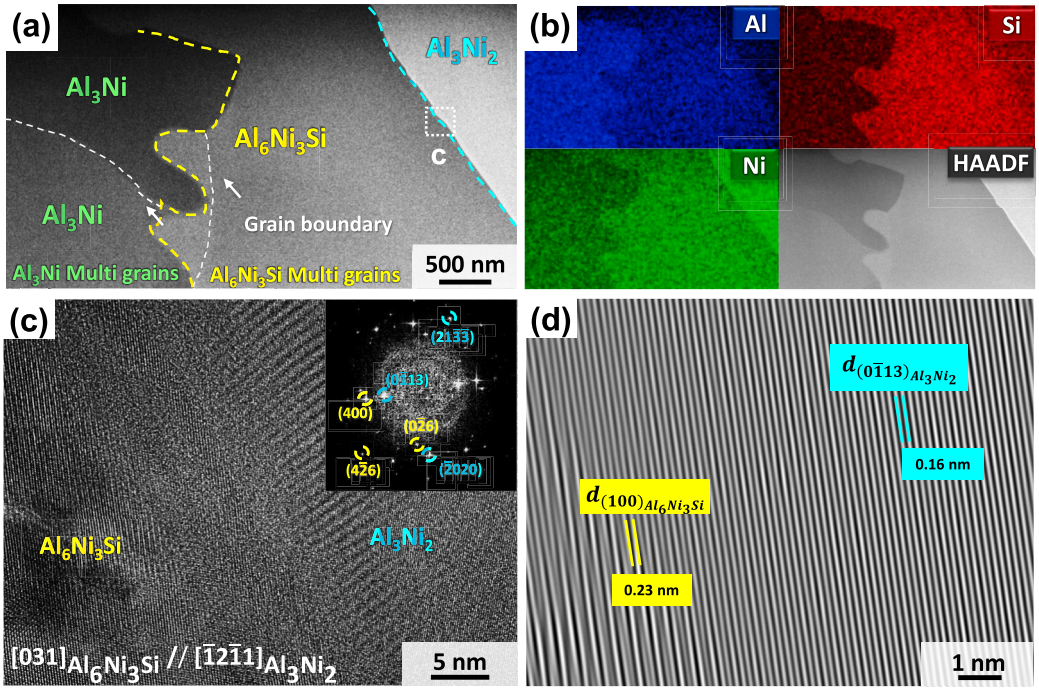

Fig. 10. (a) STEM BF image and (b) the corresponding EDS elemental maps of layered IMC particle in the 28Ni alloy with a Al_3Ni_2 core, an intermediate Al_6Ni_3Si, and an outer Al_3Ni shell (c) HR TEM image and the FFT (inset) along [031] Al_6Ni_3Si ‖ $[\bar{1}2\bar{1}1]$ Al_3Ni_2. (d) Inverse FFT image showing the interface between Al_6Ni_3Si and Al_3Ni_2 phases along (400) Al_6Ni_3Si and $(0\bar{1}13)$ Al_3Ni_2 planes.

Al_6Ni_3Si along $(0\bar{1}13)$ Al_3Ni_2 and (100) Al_6Ni_3Si. Lattice misfit calculations using Edge-to-Edge model [34,35] based on the crystallographic information (Table 2) yield an interatomic misfit of 0.65 % along the directions of $[\bar{1}2\bar{1}1]$ Al_3Ni_2 and [031] Al_6Ni_3Si (see electronic Supplementary Fig. S4). Both misfit values – (4.95 % for Al_6Ni_3Si / Al_3Ni and 0.65 % for Al_3Ni_2 / Al_6Ni_3Si) – fall well within the Edge-to-Edge model criterion (<10 %) for crystallographic coherence [34,35], validating the existence of OR between the Ni-rich IMCs. More importantly, this microstructural evidence confirms that the formation of Al_6Ni_3Si in the 28Ni alloy proceeds *via* a quasi-peritectic reaction, rather than the

conventional U-type transition reaction [24].

4.2. Diffusion-driven transformation in the Al-18Si-28Ni alloy

To further elucidate the formation of multiphase intermetallic compounds (IMCs) particularly in the 28Ni alloy, the Gibbs free energy (G) of relevant IMC phases was calculated as a function of temperature using the Thermo-Calc software and the TCAL8 database [31,36,37]. As shown in Fig. 11, within the solidification temperature range of the Al–18Si–28Ni alloy, the thermodynamic stability of the IMCs follows the order: $Al_3Ni < Al_3Ni_2 < Al_6Ni_3Si$. Notably, Al_6Ni_3Si has a substantially larger lattice volume (512.22 $Å^3$) than Al_3Ni_2 (58.16 $Å^3$) and Al_3Ni (11.45 $Å^3$) [38], providing more void space that facilitates atomic movement, lowers diffusion barriers, and enhances defect accommodation (*e.g.*, vacancies). These characteristics make Al_6Ni_3Si both energetically and structurally favorable for solid-state diffusion and phase transformation.

Richter and Isper [24] previously reported that Al_6Ni_3Si is thermodynamically stable and remains in the microstructure after annealing the sample with the nominal composition of $Al_{50}Si_{20}Ni_{30}$ (Al-15Si-48Ni in mass percent). However, under controlled cooling conditions (5 K/min) in their differential thermal analysis (DTA), this phase was not detected. Instead, a metastable phase assemblage of Al_3Ni_2, Al_3Ni, and Si was observed. They attributed this to kinetic suppression of the peritectic reaction forming Al_6Ni_3Si. However, the absence of compositional combined with crystallographic characterization in their study contrasts with the present work. The microstructure of the sample after the DTA measurement in their study closely resembles our observations in Fig. 5, suggesting that the phase they identified as Al_3Ni_2 could in fact be the more thermodynamically stable Al_6Ni_3Si. This implies that Al_3Ni_2, which forms early during solidification, may undergo a diffusion-driven transformation to Al_6Ni_3Si either during solidification. This transformation is thermodynamically favorable and, as our data suggests, kinetically feasible.

Fig. 12 provides additional evidence that the residual thickness of Al_3Ni_2 is strongly dependent on the cooling rate, increasing from 3.04 μm at 5 K/s to 57.81 μm at 50 K/s. These observations, along with thermodynamic calculations, support the reaction pathway by which the Al_6Ni_3Si is formed *via* a quasi-peritectic reaction and a diffusion reaction (Eq. (3)) as follows:

$$2Al_3Ni_2(s) + [Si] \rightarrow Al_6Ni_3Si(s) + [Ni] \quad (3)$$

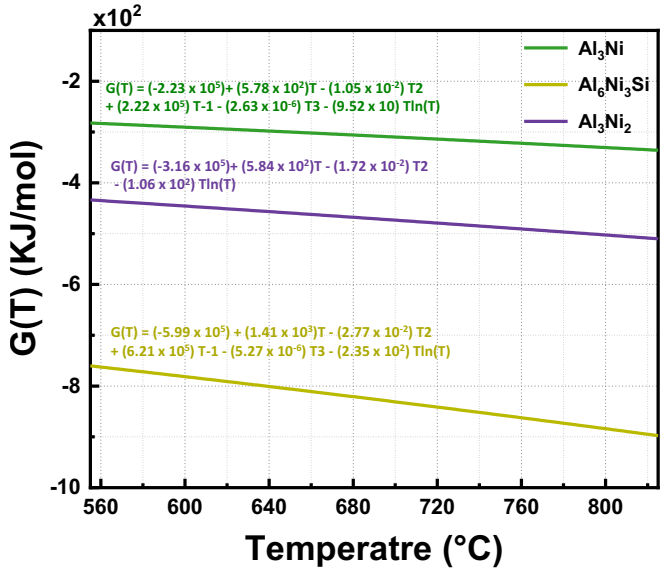

Fig. 11. Gibbs free energy of Ni-rich IMCs of the 28Ni alloy plotted as a function of temperature.

where [Si] and [Ni] are dilute solutes in liquid Al solution. As illustrated in Fig. 13, the formation of Al_6Ni_3Si starts with its nucleation onto a primary Al_3Ni_2 by the quasi-peritectic reaction (Eq. (2)), followed by the diffusion of [Si] to Al_3Ni_2 through the Al_6Ni_3Si layer and the subsequent formation of Al_6Ni_3Si *via* Eq. (3). From a kinetic point of view, it is therefore considered that the diffusivity velocity of Si in the Al_6Ni_3Si layer and the reaction velocity of Al_6Ni_3Si formation at the Al_6Ni_3Si / Al_3Ni_2 interface are essential for the complete phase transformation of Al_3Ni_2 into Al_6Ni_3Si. At very high cooling rates, for instance 50 K/s in this study, both the quasi-peritectic reaction (Eq. (2)) and the diffusion-driven reaction (Eq. (3)) are suppressed, resulting in the prevalent retention of metastable Al_3Ni_2 in the final microstructure (Fig. 12(d)).

It should be also mentioned that thermodynamic calculations predict that Al_6Ni_3Si undergoes a quasi-peritectic reaction (Eq. (1)) to form Al_3Ni and Si in the later stage of solidification (see Table 3 and Fig. 8). However, Al_6Ni_3Si is always observed in the 28Ni alloy cast at all cooling rates as shown in Figs. 5, 10 and 12. This suggests that the successive transformation from Al_6Ni_3Si to Al_3Ni is unlikely to be completed during solidification. More importantly, similar to the Al_3Ni_2 to Al_6Ni_3Si phase transformation that occurs in the early stage of solidification, the phase transformation from Al_6Ni_3Si to Al_3Ni is governed by a thermodynamically favorable quasi-peritectic reaction but kinetically limited under fast cooling conditions.

5. Conclusions

In this study, solidification behavior, microstructural evolution, and phase transformation mechanisms of Al-18Si-xNi casting alloys with varying Ni contents up to 28 wt% were systematically investigated:

1. For Ni contents ranging from 4 to 20 wt%, solidification proceeds with the sequential formation of Si_p and primary Al_3Ni, followed by a ternary Al-Si-Al_3Ni eutectic reaction.
2. When the Ni content exceeds 20 wt%, primary Al_6Ni_3Si forms first, followed by the nucleation of Al_3Ni multi grains surrounding it, resulting in a core-shell morphology. TEM observations identified a crystallographic orientation relationship (OR) between Al_6Ni_3Si and Al_3Ni: (110)[$\bar{1}$13] Al_6Ni_3Si // (0$\bar{3}$1)[$\bar{1}$13] Al_3Ni, suggesting that Al_3Ni nucleates epitaxially on the Al_6Ni_3Si substrate *via* a quasi-peritectic reaction.
3. At Ni contents exceeding 24 wt%, distinct layered Ni-rich particles were observed, consisting of a primary Al_3Ni_2 core, an intermediate Al_6Ni_3Si layer, and an outer Al_3Ni shell. The well-defined OR of (0$\bar{1}$13)[$\bar{1}$2$\bar{1}$1] Al_3Ni_2 // (100)[031] Al_6Ni_3Si. between Al_3Ni_2 and Al_6Ni_3Si indicates the formation of Al_6Ni_3Si in the early stage of solidification occurs *via* a quasi-peritectic reaction with a crystallographically coherent interface.
4. The Al_3Ni_2 phase forms primarily at high Ni content (> 24 wt%), subsequently undergoes a diffusion-driven transformation to the thermodynamically more stable Al_6Ni_3Si phase. Thermodynamic Gibbs free energy calculations, combined with measurements of residual Al_3Ni_2 thickness, confirm the feasibility and partial incompleteness of this transformation under rapid cooling conditions.

CRediT authorship contribution statement

Yoon-Ho Lee: Visualization, Validation, Software, Methodology, Investigation, Formal analysis, Data curation, Writing – review & editing, Writing – original draft. **Saif Haider Kayani:** Validation, Data curation, Writing – review & editing. **Jung-Moo Lee:** Validation, Writing – review & editing. **Sang-Ik Lee:** Investigation, Formal analysis, Data curation. **Jae-il Jang:** Validation, Writing – review & editing. **Young-Hee Cho:** Validation, Supervision, Resources, Project administration, Funding acquisition, Conceptualization, Writing – review & editing, Writing – original draft.

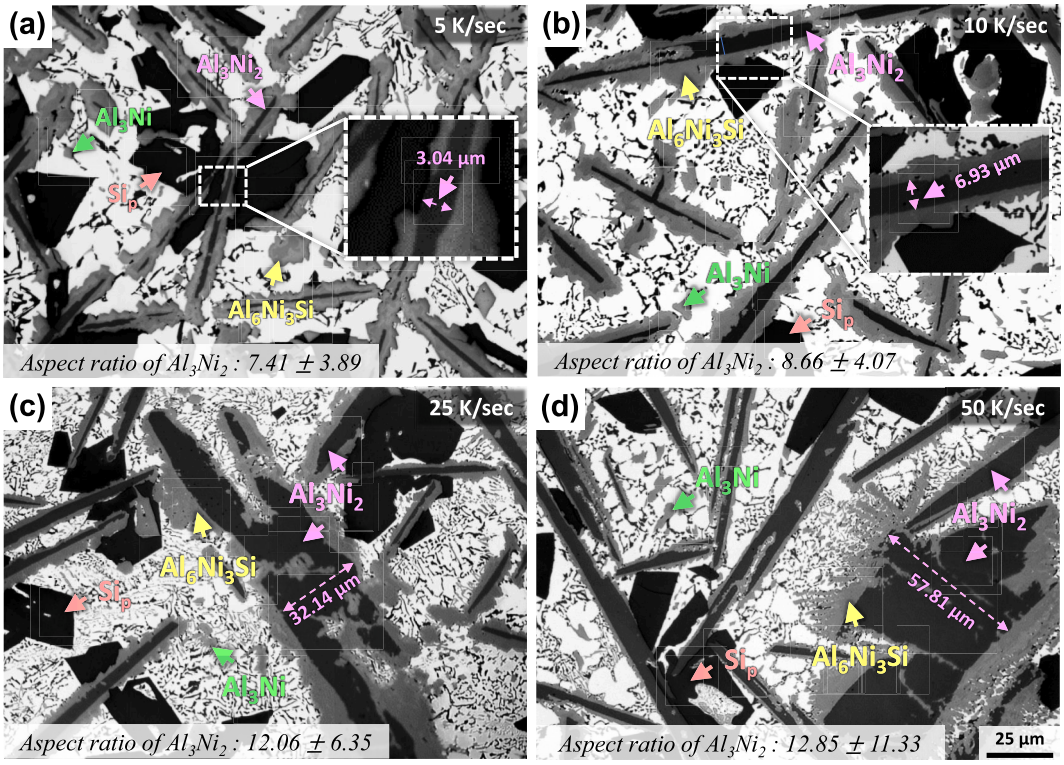

Fig. 12. Residual thickness of the Al_3Ni_2 phase in the 28Ni alloy at different cooling rates, exhibiting kinetic effects on phase retention: (a) 5 K/s; (b) 10 K/s; (c) 25 K/s; (d) 50 K/s.

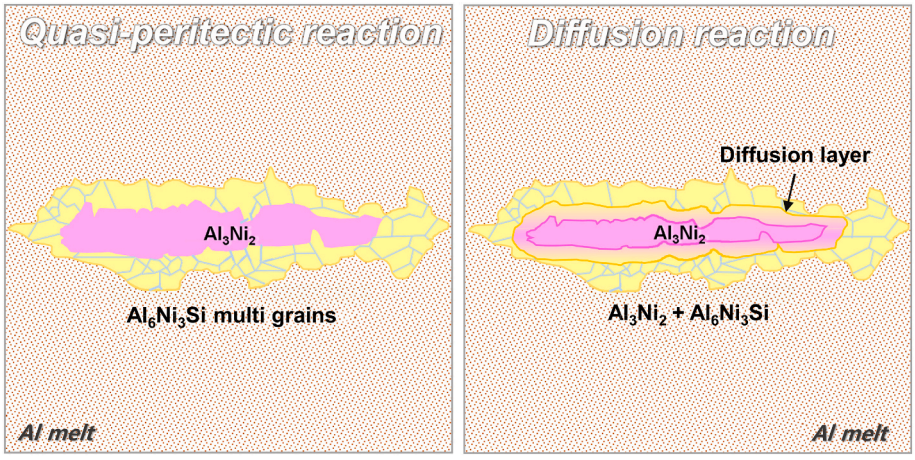

Fig. 13. Schematic illustration of the quasi-peritectic and diffusion-driven formation of Al_6Ni_3Si phase in the 28Ni alloy.

Declaration of competing interest

The authors declare that they have no known competing financial interests or personal relationships that could have appeared to influence the work reported in this paper.

Acknowledgments

This work was supported by the Industrial Technology Innovation Program (No. 20017848 and P0022331) funded by the Ministry of Trade, Industry & Energy (MOTIE, Korea).

Appendix A. Supplementary data

Supplementary data to this article can be found online at https://doi.org/10.1016/j.matchar.2025.115768.

Data availability

Data will be made available on request.

References

[1] S.H. Kayani, H.-Y. Ha, Y.-H. Cho, H.-W. Son, J.-M. Lee, Dislocation-assisted localised pitting corrosion behaviour of AlSiMgCuMn alloy, Corros. Sci. 221 (2023) 111372, https://doi.org/10.1016/j.corsci.2023.111372.

[2] X. Zhu, S. Wang, X. Dong, X. Liu, S. Ji, Morphologically templated nucleation of primary Si on AlP in hypereutectic Al-Si alloys, J. Mater. Sci. Technol. 100 (2022) 36–45, https://doi.org/10.1016/j.jmst.2021.06.009.
[3] R. Li, L. Liu, L. Zhang, J. Sun, Y. Shi, B. Yu, Effect of squeeze casting on microstructure and mechanical properties of hypereutectic Al-xSi alloys, J. Mater. Sci. Technol. 33 (2017) 404–410, https://doi.org/10.1016/j.jmst.2017.02.004.
[4] Y.-H. Lee, S.H. Kayani, J.-M. Lee, S.-I. Lee, S.-J. Kim, J.-I. Jang, Y.-H. Cho, Microstructural refinement in a high elastic modulus Al-18Si-8Ni casting alloy, J. Alloys Compd. 1008 (2024) 176580, https://doi.org/10.1016/j.jallcom.2024.176580.
[5] J.C. Williams, E.A. Starke Jr., Progress in structural materials for aerospace systems, Acta Mater. 51 (2003) 5775–5799, https://doi.org/10.1016/j.actamat.2003.08.023.
[6] R. Kasama, H. Iwaoka, Y. Umeda, T. Yongpeng, S. Hirosawa, H. Watanabe, M. Fujita, Considerable improvement in elastic moduli and the underlying mechanism of Al-cu-Zn alloy subjected to aging treatments, Materialia 14 (2020) 100911, https://doi.org/10.1016/j.mtla.2020.100911.
[7] L. Yuan, M. Guo, Z. Liu, L. Zhuang, Enhanced stiffness of Al–Zn–Mg–cu alloys via heterogeneous structure of soft and hard microdomains, Mater. Sci. Eng. A 841 (2022) 143028, https://doi.org/10.1016/j.msea.2022.143028.
[8] F. Lasagni, H.P. Degischer, Enhanced young's modulus of Al-Si alloys and reinforced matrices by co-continuous structures, J. Compos. Mater. 44 (2010) 739–755, https://doi.org/10.1177/0021998309347649.
[9] S. Amirkhanlou, S. Ji, Casting lightweight stiff aluminum alloys: a review, Crit. Rev. Solid State Mater. Sci. 45 (2020) 171–186, https://doi.org/10.1080/10408436.2018.1549975.
[10] S. Amirkhanlou, S. Ji, A review on high stiffness aluminum-based composites and bimetallics, Crit. Rev. Solid State Mater. Sci. 45 (2020) 1–21, https://doi.org/10.1080/10408436.2018.1485550.
[11] N. Dudzinski, The Young's Modulus, Poisson's Ratio, and Rigidity Modulus of some Aluminium Alloys, Royal Aircraft Establishment, Farnborough, 1952, pp. 49–55.
[12] Z. Asghar, G. Requena, E. Boller, Three-dimensional rigid multiphase networks providing high-temperature strength to cast AlSi10Cu5Ni1-2 piston alloys, Acta Mater. 59 (2011) 6420–6432, https://doi.org/10.1016/j.actamat.2011.07.006.
[13] D. Shi, B. Wen, R. Melnik, S. Yao, T. Li, First-principles studies of Al–Ni intermetallic compounds, J. Solid State Chem. 182 (2009) 2664–2669, https://doi.org/10.1016/j.jssc.2009.07.026.
[14] H.A. Hafez, M.M. Farag, Effect of structure on the young's modulus of Al-cu-Ni alloys, J. Mater. Sci. 16 (1981) 1223–1232, https://doi.org/10.1007/BF01033836.
[15] D.G. Eskin, L. Toropova, Tensile and elastic properties of deformed heterogeneous aluminum alloys at room and elevated temperatures, Mater. Sci. Eng. A 183 (1994) L1–L4, https://doi.org/10.1016/0921-5093(94)90913-X.
[16] S. Ji, F. Yan, Z. Fan, A high strength aluminium alloy for high pressure die casting, Light Met. 2016 (2016) 207–210, https://doi.org/10.1002/9781119274780.ch35.
[17] Y. Wang, L. Zhu, G. Niu, J. Mao, Conductive Al alloys: the contradiction between strength and electrical conductivity, Adv. Eng. Mater. 23 (2021) 2001249, https://doi.org/10.1002/adem.202001249.
[18] F. Stadler, H. Antrekowitsch, W. Fragner, H. Kaufmann, E. Pinatel, P.J. Uggowitzer, The effect of main alloying elements on the physical properties of Al–Si foundry alloys, Mater. Sci. Eng. A 560 (2013) 481–491, https://doi.org/10.1016/j.msea.2012.09.093.
[19] J. Hatch, Aluminum: Properties and Physical Metallurgy 424, American Society for Metals, 1984, pp. 1–24, https://doi.org/10.1361/appm1984p001.
[20] R. Kakitani, C.B. Cruz, T.S. Lima, C. Brito, A. Garcia, N. Cheung, Transient directional solidification of a eutectic Al–Si–Ni alloy: macrostructure, microstructure, dendritic growth and hardness, Materialia 7 (2019) 100358, https://doi.org/10.1016/j.mtla.2019.100358.
[21] V. Raghavan, Al-Ni-Si (aluminum-nickel-silicon), J. Phase Equilib. Diffus. 26 (2005) 262, https://doi.org/10.1007/s11669-005-0115-3.
[22] W. Xiong, Y. Du, R.-X. Hu, J. Wang, W.-W. Zhang, P. Nash, X.-G. Lu, Construction of the Al–Ni–Si phase diagram over the whole composition and temperature ranges: thermodynamic modeling supported by key experiments and first-principles calculations, Int. J. Mater. Res. 99 (2008) 598–612, https://doi.org/10.3139/146.101681.
[23] X. Liu, X. Zhou, L. Mo, M. Jiang, J. Du, Microstructural evolution and thermophysical properties of hypereutectic Al-22Si-xNi alloys prepared by sub-rapid solidification, J. Mater. Res. Technol. 21 (2022) 905–915, https://doi.org/10.1016/j.jmrt.2022.09.079.
[24] K.W. Richter, H. Ipser, The Al–Ni–Si phase diagram between 0 and 33.3 at.% Ni, Intermetallics 11 (2003) 101–109, https://doi.org/10.1016/S0966-9795(02)00184-X.
[25] L. Mo, X. Zhou, M. Lin, Y.-J. Zhao, J. Du, Microstructure, thermo-physical and mechanical properties of hypereutectic Al–10Ni-xSi alloys, J. Mater. Res. Technol. 29 (2024) 3437–3446, https://doi.org/10.1016/j.jmrt.2024.02.061.
[26] Y. Nykyruy, S. Mudry, Y. Kulyk, I. Shtablavyi, R. Serkiz, V. Girzhon, O. Smolyakov, Structure and phase transformations of amorphous-nanocrystalline Al-based alloy, applied, Nanoscience 10 (2020) 4385–4393, https://doi.org/10.1007/s13204-020-01340-y.
[27] K. Xu, K. Chang, M. Yu, D. Zhou, Y. Du, L. Wang, Design of novel NiSiAlY alloys in marine salt-spray environment: part II. Al-Ni-Si-Y thermodynamic dataset, J. Mater. Sci. Technol. 89 (2021) 186–198, https://doi.org/10.1016/j.jmst.2021.01.088.
[28] M. Senoo, H. Mii, I. Fujishiro, T. Fujikawa, Precise measurements of lattice compression of al, si and al-si alloys by high pressure x-ray diffractometry, Jpn. J. Appl. Phys. 15 (1976) 871, https://doi.org/10.1143/JJAP.15.871.
[29] M. Ellner, U. Kattner, B. Predel, Konstitutionelle und strukturelle untersuchungen im aluminiumreichen teil der systeme Ni-Al und Pt-Al, J. Less Comm. Metals 87 (1982) 305–325, https://doi.org/10.1016/0022-5088(82)90097-2.
[30] ASTM E1876-15, Standard test method for dynamic young's modulus, shear modulus, and Poisson's ratio by impulse excitation of vibration, ASTM Int. (2015) 1–17.
[31] Thermoalc with TCAL9 Batabase. https://thermocalc.com, 2025 (accessed 15 January.2025).
[32] FatcSage with FTlite Database. http://www.factsage.com, 2025 (accessed 22 November.2023).
[33] Y. Xu, Y. Deng, D. Casari, R.H. Mathiesen, X. Liu, Y. Li, Revealing the nucleation kinetics of primary Si particles in hypereutectic Al–Si alloys under the influence of P inoculation, J. Mater. Sci. 55 (2020) 15621–15635, https://doi.org/10.1007/s10853-020-05095-3.
[34] M.-X. Zhang, P.M. Kelly, M.A. Easton, J.A. Taylor, Crystallographic study of grain refinement in aluminum alloys using the edge-to-edge matching model, Acta Mater. 53 (2005) 1427–1438, https://doi.org/10.1016/j.actamat.2004.11.037.
[35] N. Zhong, X. Wang, Z. Guo, Y. Rong, Orientation relationships between ferrite and cementite by edge-to-edge matching principle, J. Mater. Sci. Technol. 27 (2011) 475, https://doi.org/10.1016/S1005-0302(11)60094-7.
[36] B. Ihsan, Thermochemical Data of Pure Substances, ISBN-10: 3527309934, 1995, https://doi.org/10.1002/9783527619825.
[37] O. Knacke, O. Kubaschewski, K. Hesselmann, Thermochemical Properties of Inorganic Substances, 2nd ed, Springer-Velarg, Berlin, 1991, pp. 1836–1837.
[38] CrystalMaker X. https://www.crystalmaker.com/, 2023 (accessed 28 June.2023).